Magneto-Inductive Catheter Receiver for Magnetic Resonance Imaging

Richard R. A. Syms*, *Senior Member, IEEE*, Ian R. Young, Munir M. Ahmad, Simon D. Taylor-Robinson, and Marc Rea

***Abstract*—A catheter-based RF receiver for internal magnetic resonance imaging is demonstrated. The device consists of a double-sided thin-film circuit, wrapped around a hollow catheter and sealed in place with heat-shrink tubing. Signals are detected using a resonant *LC* circuit at the catheter tip and transmitted along the catheter using an array of coupled *LC* circuits arranged as a magneto-inductive waveguide, a form of low frequency metamaterial. Coupling to a conventional RF system is accomplished using a demountable inductive transducer. Protection against external B_1 and E fields is obtained by using figure-of-eight elements with an electrical length shorter than that of an immersed dipole. The system is primarily designed for biliary imaging, can pass the biopsy channel of a side-opening duodenoscope, and is guidewire-compatible, potentially allowing clinicians to implement MR image guided procedures without changing their standard practice. Decoupling against B_1 and E fields is verified, and *in vitro* ^{1}H magnetic resonance imaging with submillimeter resolution is demonstrated at 1.5 T using phantoms.**

***Index Terms*—Microcoil, magnetic resonance imaging, magneto-inductive waveguide, metamaterial.**

I. Introduction

RADIO frequency (RF) receivers are required for high-resolution internal magnetic resonance imaging (MRI) of small vessels such as arteries and biliary ducts. Although small coils generally have low Q factors, a larger filling factor can be obtained from close coupling to the signal source, leading to a greater signal-to-noise ratio (SNR) at the price of a reduction in field of view (FOV) [1]. The earliest systems used wire-wound coils mounted on catheters [2]–[5]. Later systems have used two-wire transmission lines [6], meanderlines [7], and loopless catheter antennas [8], [9]. Considerable efforts have also been made to allow catheter visualization [10]–[13].

Internal imaging has also been carried out using inductively coupled coils, and SNR improvement over surface coils has again been demonstrated [14], [15]. However, this approach works best when the internal coil is in a fixed location and orientation (ideally with its plane near and parallel to the surface), and it may be difficult to achieve rapid matching during an investigative procedure when the coil is moving.

Despite successful results, a number of difficulties remain. The detectors require tuning, matching, and decoupling from the B_1 field of the transmitter. In addition, linear conductors immersed in tissue (a medium with high dielectric constant at RF [16]) can be heated by the E-field of the transmitter if their length allows standing-wave excitation [17], [18]. Attempts have, therefore, been made to develop MR-safe cables using chokes [19] or transformer subdivision [20], [21]. The result is an increase in complexity, making compact catheter receivers hard to construct. The difficulties are compounded in devices intended for biliary imaging, when the catheter must pass the biopsy channel of a duodenoscope and make a 90° turn on exit, but still provide a clear lumen for a guide-wire to assist with cannulation.

We have been developing an alternative approach based on flexible thin-film circuits that are wrapped around the outside of a catheter and held in place with heat-shrink tubing. If the necessary electrical features can be combined, this approach should allow batch fabrication of disposable imaging catheters. To date, we have demonstrated RF receivers with an internal coaxial output [22], and receivers with an external thin-film cable [23], [24]. In each case, double-sided patterning of copper-clad polyimide was used to combine two-turn spiral inductors with capacitors for tuning and matching. Small microfabricated coils have of course been fabricated on rigid substrates [25]–[27]. More recently, flexible substrates and capacitor integration have been investigated [28]–[31]. We have used step-and-repeat patterning to batch-fabricate continuous nonmagnetic circuits that are devoid of protrusions and long enough for endoscopic use. The quality of images obtained using *in vitro* specimens has been high. However, lack of protection has meant that the coils are sensitive to external B_1 fields, while the thin-film transmission line (a periodically defected microstrip [23]) is sensitive to E-fields.

Here, we demonstrate a thin-film catheter receiver aimed at overcoming these difficulties. The circuit again combines a resonant detector with an output cable. However, the detector is now designed for reduced sensitivity to uniform external RF magnetic fields, while a magneto-inductive (MI)

Manuscript received August 21, 2012; revised January 21, 2013, March 19, 2013, and April 6, 2013; accepted April 9, 2013. Date of publication April 12, 2013; date of current version August 16, 2013. This work was supported by the Wellcome Trust. *Asterisk indicates corresponding author*.

*R. R. A. Syms is with the Department of Electrical and Electronic Engineering, Imperial College London, London, SW7 2AZ, U.K. (e-mail: r.syms@imperial.ac.uk).

I. R. Young and M. M. Ahmad are with the Department of Electrical and Electronic Engineering, Imperial College London, London, SW7 2AZ, U.K. (e-mail: youngimarl@aol.com; m.m.ahmad@imperial.ac.uk).

S. D. Taylor-Robinson is with the Liver Unit, Division of Diabetes Endocrinology and Metabolism, Department of Medicine, Imperial College London, Paddington, London, W2 1PG, U.K. (e-mail: s.taylor-robinson@imperial.ac.uk).

M. Rea is with the Department of Radiology, Imperial College Healthcare NHS Trust, Paddington, London, W2 1NY, U.K. (e-mail: marc.rea@imperial.ac.uk).

Color versions of one or more of the figures in this paper are available online at http://ieeexplore.ieee.org.

Digital Object Identifier 10.1109/TBME.2013.2258020

0018-9294 © 2013 IEEE

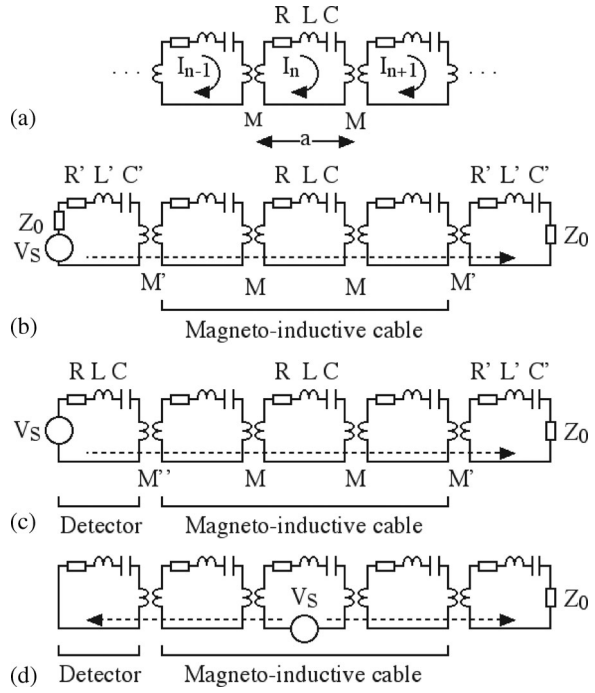

Fig. 1. Equivalent circuits for a) MI cable, b) link, c) receiver in detection mode, and d) receiver in catheter visualization mode.

waveguide [32]–[34] is used for signal transmission to avoid electrical heating. MI waveguides are a form of low frequency metamaterial and have a low-loss cable format [35] that is insensitive to bending [36] and can connect to real impedance using simple transducers [37]. Transformer-segmented MR-safe cables are variants of MI waveguides [38]. The system is intended for endoscopic delivery, is guide-wire compatible, and is provided with a demountable connector for additional safety. The receiver is designed for ^{1}H MRI at 1.5 T using a conventional clinical scanner. Methods and materials are described in Section II, and the results of mechanical and electrical characterization are presented in Section III, together with a verification of decoupling and a demonstration of MRI. Conclusions are drawn in Section IV.

II. Methods and Materials

A. Design

Fig. 1(a) shows an MI waveguide, a periodic array of low-frequency *LC* resonators with internal resistances R, coupled together by mutual inductances M.

Here, I_n is the current in the nth element. Assumption of wave solutions $I_n = I_0 \exp(-jnka)$, where I_0 is the wave amplitude, k the propagation constant, and a the period, leads to the dispersion relation

$$(1 - \omega_0^2/\omega^2 - j/Q) + \kappa \cos(ka) = 0. \quad (1)$$

Here, $\omega_0 = 1/\sqrt{(LC)}$ is the angular resonant frequency of the elements, and $Q = Q_0\omega/\omega_0$, where $Q_0 = \omega_0 L/R$ is the Q-factor. Generally, the propagation constant is complex. Writing $k = k' - jk''$, equating real and imaginary parts and assuming k'' is small, one obtains

$$(1 - \omega_0^2/\omega^2) + \kappa \cos(k'a) = 0$$
$$k''a = 1/\{\kappa Q \sin(k'a)\}. \quad (2)$$

The upper equation is the dispersion relation for loss-less MI waves. For positive κ, propagation is allowed only over the frequency band $1/\sqrt{(1+\kappa)} \le \omega/\omega_0 \le 1/\sqrt{(1-\kappa)}$. $k'a$ tends to zero and π at the two band edges. The effect of finite Q-factor is to introduce loss and allow propagation out of band. The lower equation is the approximate loss variation. Loss is minimized at resonance (when $k'a \approx \pi/2$) and inversely proportional to both κ and Q_0. The characteristic impedance is $Z_0 = j\omega M \sin(ka)$ [34], which for low loss reduces to the real value $Z_{0\mathrm{M}} = \omega_0 M$ at resonance.

A link between a source and a load with real impedance Z_0 may be constructed as shown in Fig. 1(b). Here, the terminating elements are coupled to the cable via slightly different resonant loops with parameters R', L', and C' (such that $\omega_0 = 1/\sqrt{(L'C')}$ once again) via a mutual inductance M'. Provided $\omega_0 M' = \sqrt{(Z_0 Z_{0\mathrm{M}})}$, impedance matching will be achieved at resonance, and reflections minimized over the passband.

A receiver may be constructed by replacing the source with a resonant detector, as shown in Fig. 1(c). In this case, the output impedance of the source is now equal to the loop resistance (at least, for light tissue loads). Assuming the parameters of the detector are the same as the cable elements, impedance matching now requires that $\omega_0 M'' = \sqrt{(RZ_{0\mathrm{M}})}$. A matched system will clearly allow propagation of a current wave generated by an induced voltage V_S toward the load. However, a similar voltage in one of the cable elements, as shown in Fig. 1(d), will also generate a pair of waves. One will travel toward the detector, where it will be absorbed. However, the other will again travel toward the load. Although the signal amplitude will be lower for each individual wave, the cable will, therefore, provide an imaging capability along its entire length. In this respect, the design is similar to the twisted pair receiver of Burl [10]. However, the arrangement here is a cascade of coupled resonators and can be made of arbitrary length without compromising safety.

The main design tasks are to achieve low propagation loss and impedance matching. The former merely requires strongly coupled chains of high-Q resonators. The remaining details now depend on the cable used. For example, $Z_{0\mathrm{M}}$ can be made equal to standard RF system impedance (50 Ω) through careful design [35]. In this case, $\omega_0 M' = Z_{0\mathrm{M}}$, so the value of M' needed is simply M. More generally, $Z_{0\mathrm{M}}$ will not equal 50 Ω. However, if the final coupling element is removable, matching can be achieved by adjusting the number of turns and position of this element. The detector matching condition clearly requires knowledge of R; however, this may be found experimentally from the Q-factor. The arrangement needed may then be estimated geometrically, as described later.

The performance of the systems in both Fig. 1(b) and (c) may be simulated by solving the circuit equations numerically and extracting the transmission and reflection efficiencies. As an example for comparison with later experiments, we assume a 15-element cable with parameters $f_0 = \omega_0/2\pi = 63.8$ MHz,

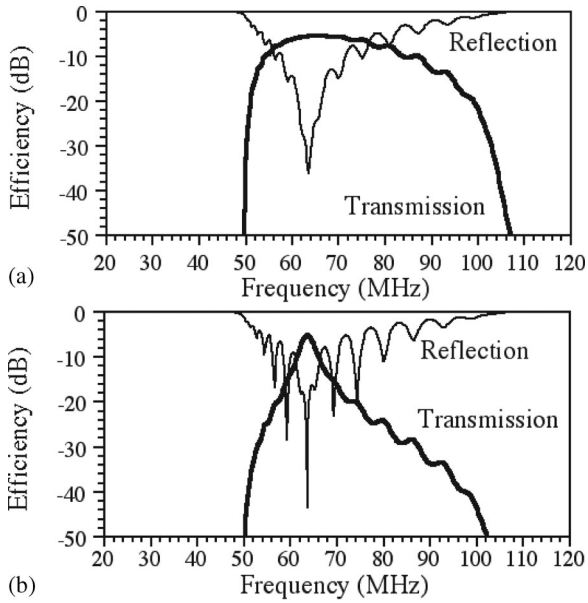

Fig. 2. Theoretical frequency variation of transmission and reflection, for a) link and b) catheter receiver.

$Q_0 = 40$, $\kappa = 0.63$, and $Z_{0\mathrm{M}} = 40\ \Omega$. We also assume that the inductance of the terminating elements is $L' = 1.6\ L$, but has a similar Q-factor. Fig. 2(a) shows the frequency response of the link. The link allows transmission over a limited passband, with a loss of around 6 dB at the resonant frequency f_0. The system is matched at f_0, but resonances can be seen elsewhere. These correspond to standing modes within the passband. Fig. 2(b) shows the corresponding plot for the detector. Transmission is again restricted to the MI band, but peaks at f_0, implying that the system is acting as a resonant detector.

B. Physical Implementation

Practical implementation requires an intrinsically safe format capable of integration on a catheter without additional components. Fig. 3(a) shows the design of a single resonant element. The inductors are single-turn loops, with a figure-of-eight layout for protection against uniform B_1 fields. The loop width is πr, so that the conductors are diametrically opposed when wrapped around a catheter of radius r. The loop length $2a$ is less than the critical length at which standing wave heating of an immersed element can be induced by an external E-field (around 28 cm for ^{1}H MRI at 1.5 T [18]). The ends of the inductors are connected to a pair of capacitor plates, which lie parallel to the conductors. A second pair of plates is provided on the rear of the substrate. Overlay yields a resonant loop containing two inductors (of value L/2) and two capacitors (of value 2 C), leading to the correct series totals. No vias or airbridges are needed to complete the circuit.

Fig. 3(b) shows the complete receiver. In the cable section, the resonant elements are overlaid to their maximum extent, to minimize propagation loss. Suitable inductor dimensions were determined by a combination of experiment and simulation. The value and dimensions of the capacitor needed to set the

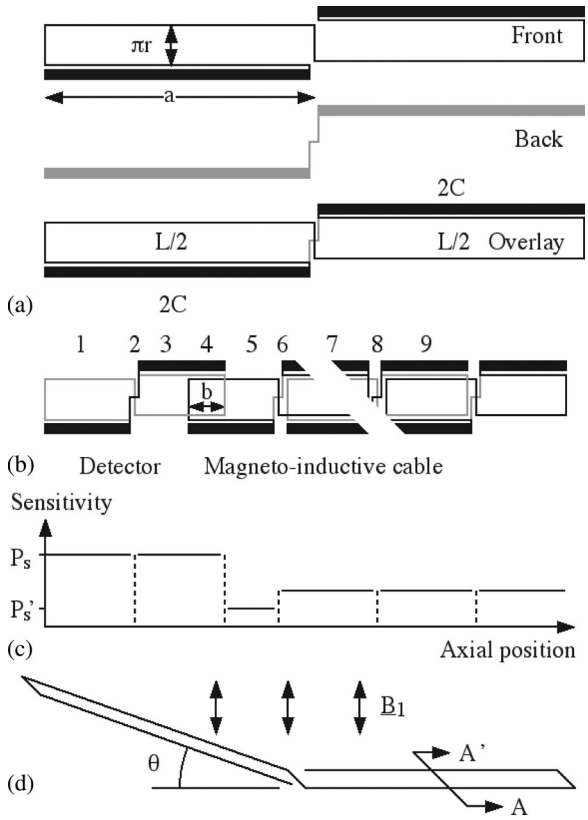

Fig. 3. Layout of a) resonant elements and b) complete receiver; c) estimated axial variation in detection sensitivity; d) abruptly-bent element.

resonance were then estimated from L, and the permittivity and thickness of the dielectric. Where necessary, the resonant frequency was tuned by trimming the capacitors. The detector is a further figure-of-eight loop, partly overlapping the final cable element. The overlap b needed for impedance matching was estimated as $b/a = \sqrt{(R/Z_{0\mathrm{M}})}$. The coupling transducer was a two-turn rectangular inductor of similar size.

To reduce friction in the 3.2 mm diameter biopsy channel of an available duodenoscope, elements were designed for mounting on a 2.25 mm diameter catheter scaffold. To pass the channel (internal length 1.4 m) and allow a working distance, cables were designed for an overall length of 1.6 m. This distance was achieved using 15 elements with an overall length of 200 mm and a period of $a = 100$ mm. Inductor track widths were 0.5 mm, and capacitors were formed using strips of 0.75 mm width. Circuits were formed in arrays of 24 off, by the U.K. company Clarydon (Willenhall, West Midlands, U.K.). The starting material consisted of 17.5 μm thickness of Cu on 25 μm thickness of Kapton HN (DuPont High Performance Films, Circleville, OH, USA). This material has excellent electrical properties. The Cu conductivity is close to that of bulk material, while the dielectric has a low loss tangent (0.006). Fabrication was carried out by step-and-repeat exposure to 2-m long photomasks, followed by development and wet etching. A similar process was used to form two-turn inductors for use as coupling transducers.

Thin-film circuits were integrated onto catheters, as shown in Fig. 4. The scaffold was a single lumen PTFE tube (Type HW16,

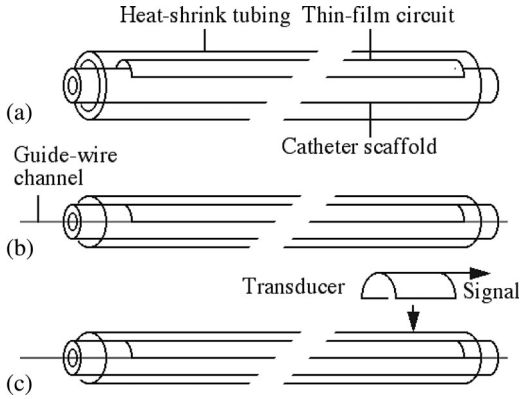

Fig. 4. Mechanical construction of catheter-based receiver.

Adtech Polymer Engineering, Stroud, Gloucester, U.K.). This material was held on a stretched wire jig. The PCB was then trimmed and mounted on the catheter with adhesive tape, as shown in Fig. 4(a). The cladding is a thin-walled polyolefin heat-shrink tube containing a plasticiser (Type SPTW, ShrinkTek Polymers Int., Cheltenham, Gloucester, U.K.). This material was passed over the catheter and heated to seal the assembly, as shown in Fig. 4(b). Inductive transducers were constructed from two-turn thin-film inductors, which were epoxied onto the inside of a split Perspex clamp equipped with a RF connector. The clamp was attached to the outside of the catheter, as shown in Fig. 4(c).

The use of identical elements for signal detection and transmission considerably simplifies development. Only the parameters of the MI waveguide are important, and their values were found from experiments. Measurement of the resonant frequency $f_0 = \omega_0/2\pi$ of isolated inductors after the addition of a known capacitor (using an Agilent E5061A network analyzer, with inductive probes for excitation and detection) allowed extraction of the self-inductance L. Similarly, measurement of the resonant frequency and Q-factor of inductors with integrated capacitors allowed the capacitance C and resistance R to be determined. Measurement of the two resonant frequencies f_1 and f_2 of the coupled system formed by pairs of elements allowed an estimate of the mutual inductance M. Suitable layouts were then achieved by iteration.

C. Axial Variation in Sensitivity

Within each element, the transverse variation in sensitivity of the receiver can be assumed to be that of a rectangular loop. The axial variation in sensitivity is more complicated. Although the equivalent circuits in Fig. 1(c) and (d) provide a broad description of signal detection, the strong overlap of the elements in Fig. 3(b) introduces some modifications. We, therefore, provide a more detailed explanation in terms of MI waves.

Consider a group of spins in position 1 in Fig. 3(b), close to the left-hand half of the detector. We shall assume these are capable of generating a voltage V_S in the loop. Assuming perfect matching and ignoring propagation loss, this voltage will excite an MI wave that carries a signal power $P_1 = V_S^2/8R = P_S$ toward the load. The same group of spins in position 2 will not generate a signal, because any induction in the left- and right-hand halves of the detector will cancel. Consequently, $P_2 = 0$. For position 3, we would expect a voltage V_S, and hence, a power $P_3 = P_S$ once again. For position 4, we would expect the same result for the detector. Here, however, the spins can also couple to the left-hand half of the first cable element. A voltage V_S induced here will lead to a pair of current waves, propagating in either direction. The wave traveling toward the detector will simply be absorbed, leaving the other carrying a signal power $P_S{}' = V_S/8Z_{0M}$ toward the load. Because $R << Z_{0M}$, $P_S{}'$ must be much less than P_S. Consequently, we can assume that $P_4 \approx P_S$ to reasonable approximation. For position 5, the signal is only induced in the first cable element. In this case, the voltage leads only to the reduced power $P_5 = P_S{}'$ in the load. Clearly, $P_6 = 0$ once again. For position 7, the signal is induced in both the first and second cable elements, generating a pair of current waves in each case. However, the waves traveling toward the load are in quadrature, so the total power carried is $P_7 = 2P_S{}'$. The remainder of the pattern repeats, with $P_8 = 0$, $P_9 = 2P_S{}'$, and so on. Thus, the expected axial variation is as shown in Fig. 3(c). Sensitivity peaks in the detector elements. There is a large reduction just beyond and a small recovery to uniform sensitivity in the cable elements.

D. Decoupling Against External Fields

Decoupling against B_1 fields will degrade when the voltages induced in each lobe of the figure-of-eight elements no longer cancel. The worst case occurs when an element is abruptly bent through an angle θ at its midpoint, as shown in Fig. 3(d). If it is oriented so that one lobe has its normal in the B_1 direction (considered fixed, for simplicity), the reduction in induced voltage compared with a similar untwisted element is $A_V = [1 - \cos(\theta)]/2$, with a corresponding power reduction of $A_P = 20 \log_{10}(A_V)$ (dB). Performance improves if the element is not bent abruptly, if it is not bent at its midpoint, or if it has a more favorable orientation. For example, if the bend occurs half-way along one lobe, A_V improves to $[1 - \cos(\theta)]/4$.

For an untwisted loop of area S oriented perpendicular to a flux density B_1 varying at ω, the induced current is $I = j\omega B_1 S/R$, where R is the loop resistance. This result can be written as $I = jB_1QS/L$, where Q is the quality factor and L is the inductance. Taking into account decoupling in a twisted loop, the current reduces to $I = jB_1QSA_V/L$. This current will generate a magnetic field. For a single conductor with a circular section, the flux is circumferential and can be found as $B_\phi = \mu_0 I/2\pi r$. B_ϕ is clearly proportional to B_1, and the radius $r = \mu_0 QSA_V/2\pi L$ at which they are comparable will determine the distance at which significant artifacts are seen. For the coils used here, $Q = 40$, $S = 200 \times 3 \times 10^{-6}\text{m}^2$, $L = 0.275 \times 10^{-6}\text{H}$, and hence, $r = 0.01745\ A_V$ m. This analysis leads to the data in Table I, which suggest that the decoupling will be effective and the artifact range small at least till $\theta = 30°$, and to larger angles in more gradual bends.

Several authors [20], [21] have commented on the need for low parasitic capacitance between sections in transformer-segmented lines, since this will allow ac common-mode current

TABLE I
DEPENDENCE OF VOLTAGE ATTENUATION A_V, POWER ATTENUATION A_P, AND ARTIFACT RADIUS r ON THE ANGLE θ IN ABRUPTLY BENT COILS

θ (deg)	A_V	A_p (dB)	r (mm)
10	0.007	-42.39	0.13
20	0.030	-30.41	0.53
30	0.067	-23.48	1.17
45	0.146	-16.69	2.55
60	0.250	-12.04	4.36

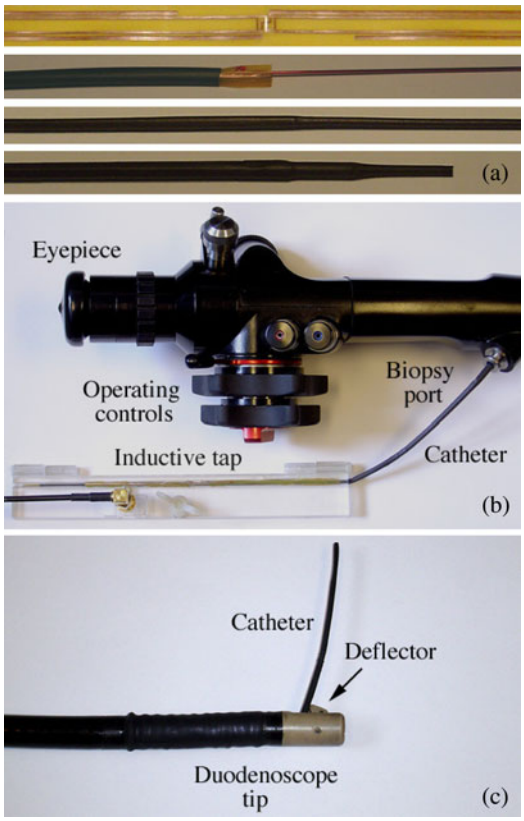

Fig. 5. a) Stages in construction of catheter-based receiver; b) receiver with demountable transducer attached and passing into the biopsy channel of a nonmagnetic duodenoscope; c) receiver passing from the side-port.

induced by external E-fields to flow across the boundaries between elements. We cannot eliminate this capacitance, but have minimized its effect by staggering the conductors of adjacent elements laterally as shown in Fig. 3(b), so they do not overlay exactly.

III. RESULTS

A. Assembly and Mechanical Evaluation

Visual inspection showed that the circuits were printed reliably, with good front-to-back alignment. Construction required removal of excess material from PCB edges, and the use of Kapton tape to fix the circuit while the heat-shrink sleeve was applied. Care was needed to ensure the PCB was coaxially aligned, and that sheathing did not introduce folds. Fig. 5(a) shows stages in catheter integration, namely a section of cable (top), a partly sheathed catheter, a fully sheathed catheter, and a completed receiver (bottom).

Completed catheters were mechanically flexible. However, the cable layout places conductors at some distance from the neutral axis, resulting in an increase in bending stiffness over that of the scaffold. One solution might be a meandered layout. Fig. 5(b) shows the proximal end of completed catheter receiver with the demountable transducer attached and passing into the biopsy channel of a nonmagnetic duodenoscope designed for interventional MRI (Endoscan, London, U.K.). Fig. 5(c) shows the distal end of the catheter emerging from the side-port at the tip. The catheter is clearly small and flexible enough to pass the biopsy channel. However, careful insertion was required to avoid buckling. Some damage to the heat-shrink was also noted on retraction, caused by an internal joint between sections of the biopsy channel. Further work is, therefore, required to develop a system for clinical use.

B. Electrical Evaluation

Component values appeared extremely repeatable. Measurement of the resonant frequencies of eight isolated cable elements yielded a standard deviation of 0.7%. Catheter mounting resulted in a mean increase in resonant frequency f_0 of 4%, caused by the deformation of the inductor shape. However, catheter mounting caused a mean reduction in the ratio M/L of only 2%, to around 0.315.

Parameter extraction led to design values for catheter-mounted cables and resonant detectors operating at 63.85 MHz. Fig. 6(a) shows the electrical response of a catheter-mounted link. These results should be compared to Fig. 2(a); the results are in reasonable agreement, but the transmission is around 2 dB lower and falls more rapidly at higher frequency. The main reasons are likely to be frequency dependence of loss in the conductor, loss in the dielectric and parasitic capacitance, all of which are omitted from the simple model.

Fig. 6(b) shows the response of a completed catheter receiver. These results should be compared to Fig. 2(b). In this case, a separate inductive loop was used to transfer the signal between the detector and the ENA, so the peak transmission (S_{21}) is approximately 15 dB lower. However, there is again generally good agreement. The operating frequency is set to better than 1 MHz, and a loaded Q-factor approaching 30 is obtained. The deep trough in the frequency variation of the reflection (S_{11}) confirms that impedance matching has been achieved.

The axial variation in sensitivity was assessed electrically, by measuring the signal at 63.85 MHz as the loop was moved along the catheter. The results are shown in Fig. 6(c) and should be compared with Fig. 3(c). Sensitivity is high at the resonant detector, then falls abruptly, and finally climbs again as losses reduce toward the tap. Losses in the cable section can be extracted as 7–8 dB. For comparison, the loss of an equivalent length of subminiature coaxial cable (0.8 mm dia, Axon Cable Ltd., Dunfermline, U.K.) was measured as $\approx$1 dB, illustrating the loss penalty of the construction.

Performance was stable against variations in operating condition. Fig. 7(a) shows the frequency dependence of the transmission before and after a nitinol biliary cannulation guidewire

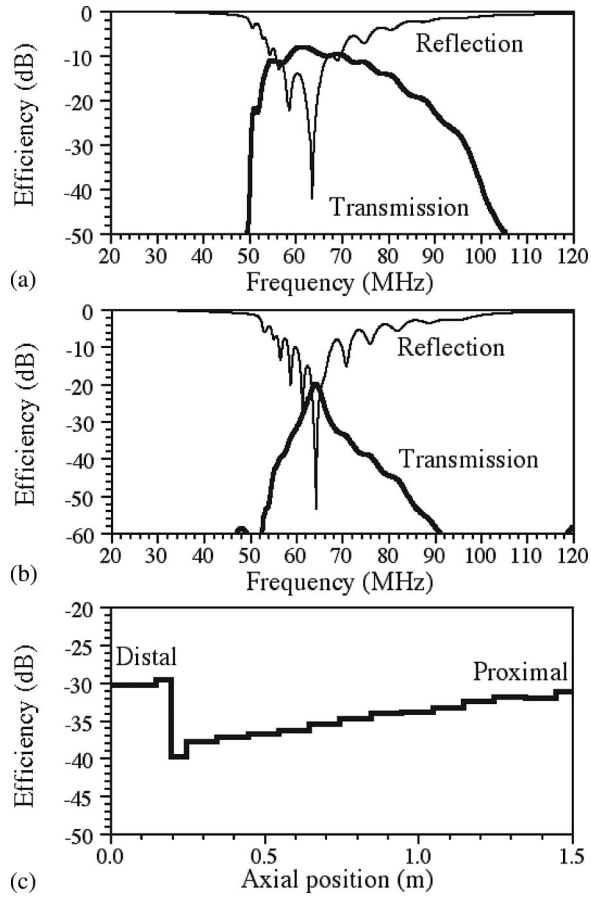

Fig. 6. Experimental frequency variation of transmission and reflection for a) link and b) receiver; c) axial variation in sensitivity.

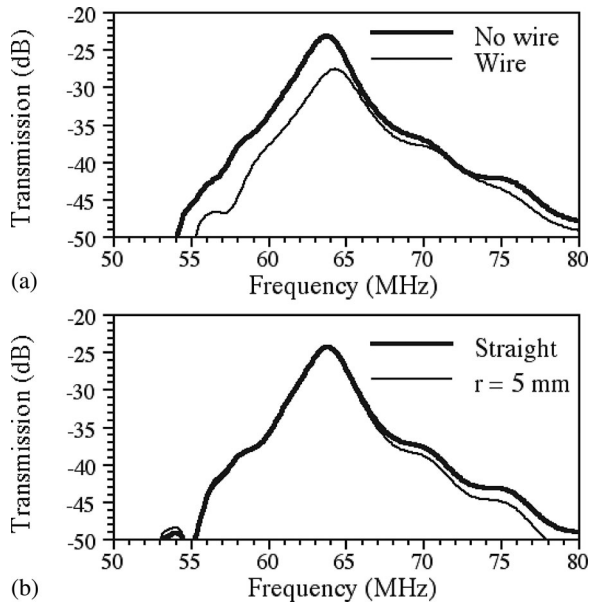

Fig. 7. Experimental frequency-dependence of transmission for receiver: a) before and after insertion of a guidewire and b) before and after bending through 90° round a radius of 5 mm.

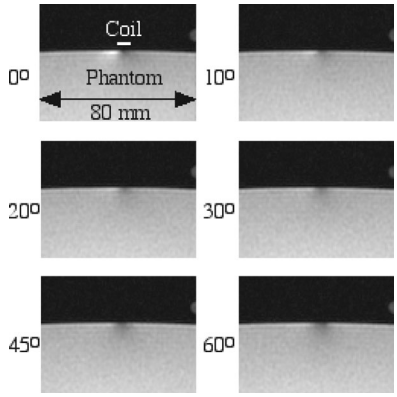

Fig. 8. Axial images obtained in the arrangement of Fig. 3(d) for different bend angles θ.

(Hydra Jagwire, Boston Scientific, Natick, MA, USA) was inserted into the catheter lumen. The wire shifts the resonant frequency of the system upward, by around 1 MHz and reduces the Q-factor to around 20; however, the response is otherwise relatively unaffected.

Fig. 7(b) shows the transmission before and after bending the detector through 90° around a plastic mandrel of radius 5 mm, used to mimic delivery from the side-port of a duodenoscope. There is little difference in the results. However, the effect of repetitive bending during clinical use has yet to be investigated. RF signals were also transmitted along a catheter fully immersed in the duodenoscope. Once again, a reduction in Q-factor to ≈ 20 was observed, which was traced to the presence of a curved metal section within the biopsy channel. Further work is required to improve electrical compatibility between the duodenoscope and catheter.

C. Magnetic Resonance Imaging

^{1}H MRI was carried out at St. Mary's Hospital, Paddington, London, U.K., using a 1.5 T Signa Excite clinical scanner (GE, Milwaukee, WI, USA). For the reasons given above, imaging was carried out using phantoms in place of the duodenoscope. The initial phantoms were cuboids filled with a solution containing 3.37 g/L $NiCl_2.6H_2O$ and 2.4 g/L NaCl (with $T1 =$ 500–800 ms and $T2 =$ 100–200 ms), which were arranged parallel to the magnet bore.

B_1-field decoupling was first verified using an unmounted element, which was placed on a cuboid phantom, and bent through an angle θ at its midpoint in the arrangement of Fig. 3(d) using a balsa-wood ramp. Axial images were then obtained using the body coil along the length of the first section, which remained in contact with the phantom. Imaging was carried out using a fast spoiled gradient recalled echo (GRE) sequence with TR = 68 ms, TE = 2.752 ms, 10 mm slice thickness, 11 mm slice separation, 200 mm FOV, and four averages to improve SNR. Fig. 8 shows a composite axial image along the line A-A' for 30° flip angle. The phantom is the lower bright region in each case. A small perturbation, ascribed to currents flowing in the

capacitor, can be seen as a shallow, off-center bright spot for $\theta = 0°$. As θ increases toward 60°, this spot is gradually augmented with a deeper symmetric dark area, due to imbalance between the currents in the two halves of the coil. All perturbations are short-range, and it was not possible to achieve more dramatic results. The same pattern was seen at flip angles of 10° and 20°. B_1 coupling effects, therefore, appear consistent and are small even with abrupt, large-angle bends.

E-field decoupling was then investigated, using experiments aimed at establishing the potential for electrically induced heating. Four MI cables of different lengths (200, 300, 400, and 500 mm, corresponding to 1, 2, 3, and 4 loops) straddling the critical resonant length were tuned for operation at 63.85 MHz and mounted on separate catheters. The four cables were suspended in an array, which was placed at the center of a long trough with a cross section of 50 mm × 50 mm. To provide an appropriately surrounding medium, the trough was filled with a saline solution (0.7 g/L Na Cl, with a conductivity of 0.26 S/m), thickened to a viscous gel with polyacrylic acid (8 g/L PAA) to prevent convection. A STF-10M fiber-optic temperature probe (Lumasense Technologies Inc., Santa Clara, CA, USA) was attached to the midpoint of each cable, and the fibers were routed to a four-channel Luxtron FOT Lab Kit interfaced to a PC.

RF heating was carried out using the scanner, with the body coil acting as a transmitter. The trough was placed on the patient bed in several positions (on the midline, and close to the body coil) and orientations (conductors parallel to the magnet bore, and arranged obliquely). Heating was carried out using an RF-intensive FIESTA sequence, with flip angle up to 120°, a repeat time TR = 8 ms and an echo time TE = 2.3 ms. Repetitive imaging was carried out, for up to 10 min in each arrangement. The cables were visible due to the incomplete decoupling from B_1 fields. However, no statistically significant temperature changes were observed, in any arrangement, apart from a slow cooling of the gel as it adjusted to the temperature of the magnet room. The experiments were then repeated with the fiber optic probes close to the cable ends, with similar null results.

Image quality was then investigated using a catheter coil, which was taped on top of the phantom with its axis parallel to the magnet bore. The system body coil was used for excitation, and the catheter was connected to an auxiliary coil input for signal reception. No additional protection was provided against direct coupling to the transmitter. Despite this, no damage to the thin-film PCB was observed.

Fig. 9(a) shows a coronal localizer image obtained using the body coil for signal reception. Here, the majority of the cuboid phantom can be seen, but the catheter is largely invisible. Its track is only indicated by a residual perturbation to the local magnetization. However, the effect is minor, confirming that the figure-of-eight shaped elements do indeed provide effective cancellation of directly induced signals.

Fig. 9(b) shows a coronal image obtained using the catheter coil. Here a 2-D GRE sequence was used, with an echo time $TE = 2.78$ ms, a repetition time $TR = 68$ ms, a flip angle of 30°, a 5 mm slice thickness, and a 400 mm FOV. Four averages were used to improve SNR. The image is now obtained only in the immediate vicinity of the catheter. The tip is clearly visible

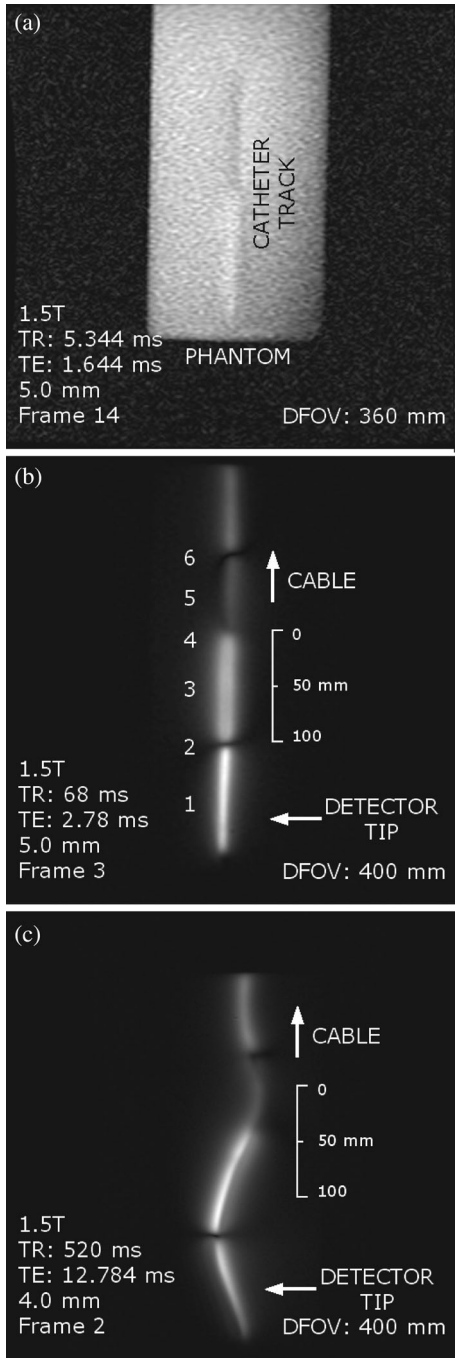

Fig. 9. ^{1}H MR images of cuboid phantom: a) coronal localizer; b) and c) coronal catheter-coil images with catheter straight and meandered, respectively.

as a pair of rectangular bright lobes [locations 1 and 3–4, previously shown in Fig. 3(b)], each around 100 mm long and separated by a darker region 2 where the coil windings cross. At its brightest point, the SNR of the image is ≈ 95. Imaging is also achieved along the cable; however, as expected, the signal is weaker here. Particularly, the signal is much weaker in section 5 immediately following the detector, as predicted in Section II-C. Fig. 9(c) shows a similar image obtained with a slightly different sequence, with the catheter now held in a meandered track,

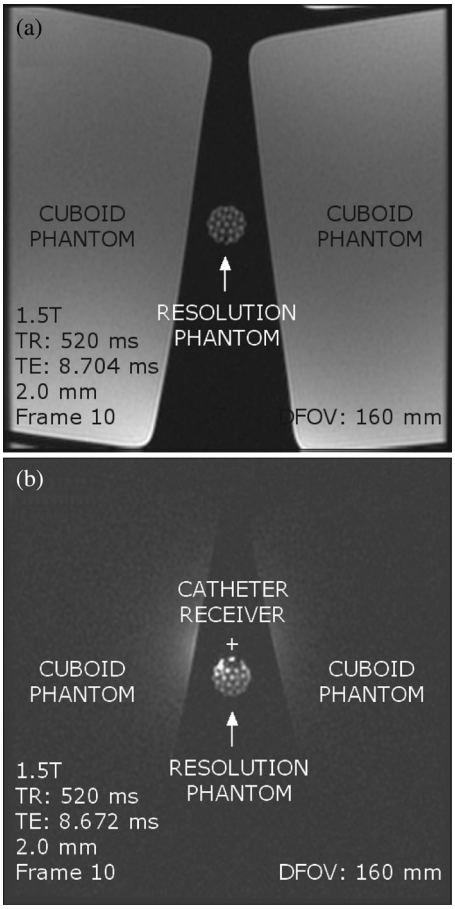

Fig. 10. Axial ^{1}H MR images obtained using a) an eight-element array and b) the catheter receiver; c) high-resolution image obtained using the catheter.

showing that the catheter can still provide high-quality images when significantly distorted.

Further imaging was then carried out using a phantom designed to evaluate the potential for high-resolution imaging in the body. This phantom was a small (1.7 cm ID) cylinder filled with the same solution of $NiCl_2$ and NaCl, and containing immersed nylon tubes to provide structure. The resolution phantom was sandwiched between two cuboids used to represent body loading. A comparison was then made between the performance of an eight-element GE HD cardiac array coil and the catheter receiver (which was placed on top of the resolution phantom). Fig. 10(a) shows an axial slice image obtained using the array. Here, a 2-D spin echo sequence was used, with $TR = 520$ ms, $TE = 8.704$ ms, 90° flip angle, 2 mm slice thickness, 2.2 mm slice spacing, and 160 mm FOV. Four averages were used to improve SNR, and 19 slices were acquired in 2 min and 49 s. The two cuboids are clearly visible on the LHS and RHS, with the resolution phantom between. The image brightness is generally uniform, increasing slightly near the array elements. Fig. 10(b) shows the corresponding image obtained using the catheter receiver, with the same parameters. The restricted FOV of the catheter receiver is immediately apparent, as is a small artifact immediately beneath it.

TABLE II
COMPARISON BETWEEN THE SNR ACHIEVED USING THE CATHETER RECEIVER AND AN EIGHT-ELEMENT CARDIAC ARRAY, AVERAGED OVER THE RESOLUTION PHANTOM

Coil	FOV(mm)	Averages	Time	SNR
Array	80	1	44 s	7.7
Catheter	80	1	44 s	5.7
Array	80	4	2 m 49 s	12.5
Catheter	80	4	2 m 49 s	10.2
Array	160	4	2 m 49 s	39.8
Catheter	160	4	2 m 49 s	37.5

Due to its nonuniform reception pattern, the SNR achievable using the catheter receiver must depend on distance. However, the corresponding SNR of the array coil should not vary significantly. As a result, although the catheter receiver may have a local SNR advantage, this must sooner or later be lost. Comparative SNR values were computed by assuming the whole of the resolution phantom as the region of interest (ROI) for signal, and rectangular areas on either side as the ROI for noise. The results are shown in Table II. The data are consistent and show that the catheter receiver can achieve similar performance to the array over a useful FOV, a significant achievement for such an embryonic device. Further improvements are likely to follow if propagation losses can be reduced and artifacts can be controlled.

The principle of MR imaging during endoscopy was then demonstrated using a nonfunctioning model of the duodenoscope. This component was constructed from nonmagnetic materials (polyether ether ketone, or PEEK and polyoxymethylene, or Delrin) and consisted of the instrument tip, a section of biopsy channel, and a deflector lever. An imaging catheter was passed through the channel, so that its tip emerged at right angles. The combination was immersed in a tank filled with the $NiCl_2$/NaCl solution, arranged as shown in Fig. 11(a). As before, the body coil was used for excitation, and similar sequences were used. Images were obtained using two averages and an acquisition time of 2 min 13 s. Fig. 11(b) shows a sagittal slice image obtained using the body coil, in which the dummy tip, deflector, and catheter receiver can all be seen against a signal background provided by the immersion liquid. There is some overexcitation near the catheter, presumably because the decoupling is less effective with a curved path. The image is noisy, with an SNR of only 5.6. Using the same sequence parameters, but with additional phantoms to simulate body loading, the SNR obtained using the surface coil array was 16.

Fig. 11(c) shows a similar image obtained using the catheter receiver. The FOV is clearly much lower, but the catheter provides uniform imaging along its length, despite the bend at the exit from the tip. However, the sensitivity of the catheter receiver falls off with radial distance. The local variation of SNR was, therefore, assessed using large noise ROIs in the corners of the image and small signal ROIs measuring 5×1 pixels, moving away from the catheter tip in steps of 1 pixel as shown. The following SNR values were obtained for the eight signal

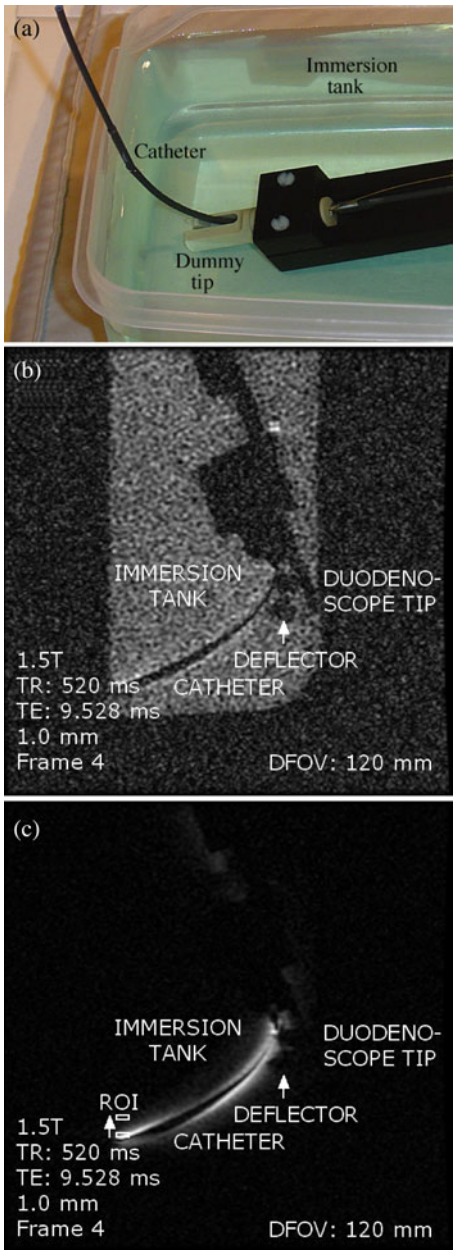

Fig. 11. a) Duodenoscope phantom, b) and c) sagittal images of the immersed phantom obtained using the body coil and catheter coil, respectively.

ROIs nearest the catheter: 70, 52, 36, 26, 20, 14, 10, and 9.5. With the pixel size here (0.4688 mm), these results suggest that the catheter can provide much better local performance than the array at ($>4\times$) at short distance, and equivalent performance to a distance of at least 2 mm in realistic circumstances. Averaging SNR data over a larger area, as was done in Table II, typically provides an over estimate of the useable FOV.

Although these results are some way from human imaging, they clearly demonstrate the new principle of this research, namely detection and transmission of MR images via an entirely printed safe structure that can be applied to a catheter device without affecting its normal operation.

IV. Conclusion

We have demonstrated a novel catheter-based receiver for internal MRI, entirely constructed from a single thin-film printed circuit mounted on a hollow catheter scaffold. The circuit consists of a cascade of magnetically coupled inductor loops made resonant with integrated capacitors. Detection of RF signals is achieved by excitation of MI waves. Inherent protection against the E-field and B_1-field of the transmitter is achieved through transformer subdivision and the use of figure-of-eight resonant elements, respectively. Frequency tuning is carried out by trimming the capacitors, while impedance matching to the detector and the load is achieved by transformer coupling. The system has been designed for operation at 63.85 MHz. However, scaling to other frequencies should be possible, by alteration of the element length.

The system is primarily designed for improving the resolution of imaging at biliary endoscopy, where there is a pressing clinical need owing to the increased prevalence of bile duct tumours. However, further possible applications include imaging of other luminal gastrointestinal diseases, including oesophageal, gastric and pancreatic pathology, intraarterial imaging of major organs including the brain and cardiac imaging. The catheter is guidewire compatible, and small and flexible enough to pass the biopsy channel of a side-opening duodenoscope. The catheter is hermetically sealed and has shown encouraging tolerance to bending. However, further work is required to improve flexibility, confirm reliable operation under the repetitive bending likely to occur during cannulation, and improve duodenoscope compatibility.

Preliminary demonstration of ^{1}H MRI has been made at 1.5 T using phantoms. The system provides sensitive detection up to the catheter tip, and detection with reduced sensitivity along the catheter length. However, improvements to the MR-safe cable and its immediate electrical environment are required to reduce propagation losses.

Further improvement to the decoupling may also be required to reduce artifacts, especially at the resonant tip. On possibility is optical decoupling [39], using a waveguide to transfer an optical signal along the cable and hence control a photodiode arranged in parallel with one of the capacitors in the distal loop. Catheter-integrated, optically detunable resonant markers with a fiber feed have already been demonstrated [40]; here, the challenge would be to combine a printed polymeric waveguide with the thin-film electrical circuit, together with a hybrid integrated photodiode.

Finally, further investigation of residual heating effects is also required before any *in vivo* imaging can take place. This work is in progress. Subsequent, and finally human, studies are being pursued, although ethical permissions are a substantial source of delay.

Acknowledgment

The authors are extremely grateful to Prof. W. Gedroyc for scanner access, to Clarydon for provision of thin-film PCBs, and to Endoscan Ltd. for endoscope components. Valuable discussions with M. Ristic, L. Solymar, and K. Shamonina are also gratefully acknowledged.

REFERENCES

[1] P. A. Bottomley, E. Atalar, R. F. Lee, K. A. Shunk, and A. Lardo, "Cardiovascular MRI probes for the outside in and for the inside out," *Magn. Reson. Mats. Phys. Biol. Med.*, vol. 11, pp. 49–51, Nov. 2000.

[2] H. L. Kantor, R. W. Briggs, and R. S. Balaban, "In vivo ^{31}P nuclear magnetic resonance measurements in canine heart using a catheter-coil," *Circ. Res.*, vol. 55, pp. 261–266, Aug. 1984.

[3] G. C. Hurst, J. Hua, J. L. Duerk, and A. M. Cohen, "Intravascular (catheter) NMR receiver probe: Preliminary design analysis and application to canine iliofemoral imaging," *Mag. Reson. Med.*, vol. 24, pp. 343–357, Apr. 1992.

[4] K. Kandarpa, P. Jakab, S. Patz, F. J. Schoen, and F. A. Jolesz, "Prototype miniature endoluminal MR imaging catheter," *J. Vasc. Interv. Radiol.*, vol. 4, pp. 419–427, May/Jun. 1993.

[5] D. Crottet, R. Meuli, S. Wicky, and J. J. van der Kink, "Reciprocity and sensitivity of opposed-solenoid endovascular MRI probes," *J. Magn. Reson.*, vol. 159, pp. 219–225, Dec. 2002.

[6] E. Atalar, P. A. Bottomley, O. Ocali, L. C. L. Correia, M. D. Kelemen, J. A. C. Lima, and E. A. Zerhouni, "High resolution intravascular MRI and MRS by using a catheter receiver coil," *Magn. Reson. Med.*, vol. 36, pp. 596–605, Oct. 1996.

[7] C. T. Farrar, V. J. Wedeen, and J. L. Ackerman, "Cylindrical meander-line radiofrequency coil for intravascular magnetic resonance studies of atherosclerotic plaque," *Magn. Reson. Med.*, vol. 53, pp. 226–230, Jan. 2005.

[8] O. Ocali and E. Atalar, "Intravascular magnetic resonance imaging using a loopless catheter antenna," *Magn. Reson. Med.*, vol. 37, pp. 112–118, Jan. 1997.

[9] R. C. Susil, C. J. Yeung, and E. Atalar, "Intravascular extended sensitivity (IVES) MRI antennas," *Magn. Reson. Med.*, vol. 50, pp. 383–390, Aug. 2003.

[10] M. Burl, G. A. Coutts, D. Herlihy, R. Hill-Cottingham, J. E. Eastham, J. V. Hajnal, and I. R. Young, "Twisted-pair RF coil suitable for locating the track of a catheter," *Magn. Reson. Med.*, vol. 41, pp. 636–638, Mar. 1999.

[11] Q. Zhang, M. Wendt, A. J. Aschoff, J. S. Lewin, and J. L. Duerk, "A multielement RF coil for MRI guidance of interventional devices," *J. Magn. Reson. Imag.*, vol. 14, pp. 56–62, Jul. 2001.

[12] S. Zuehlsdorff, R. Umathum, S. Volz, P. Hallscheidt, C. Fink, W. Semmler, and M. Bock, "MR coil design for simultaneous tip tracking and curvature delineation of a catheter," *Magn. Reson. Med.*, vol. 52, pp. 214–218, Jul. 2004.

[13] C. M. Hillenbrand, D. R. Elgort, E. Y. Wong, A. Reykowski, F. K. Wacker, J. S. Lewin, and J. L. Duerk, "Active device tracking and high-resolution intravascular MRI using a novel catheter-based opposed solenoid phased array coil," *Magn. Reson. Med.*, vol. 51, pp. 668–675, Apr. 2004.

[14] M. D. Schnall, C. Barlow, V. H. Subramanian, and J. S. Leigh, "Wireless implanted magnetic resonance probes for *in vivo* NMR," *J. Magn. Reson.*, vol. 68, pp. 161–167, Jun. 1986.

[15] E. D. Wirth, T. H. Mareci, B. L. Beck, J. R. Fitzsimmons, and P. J. Reier, "A comparison of an inductively coupled implanted coil with optimized surface coils for *in vivo* NMR imaging of the spinal cord," *Magn. Reson. Med.*, vol. 30, pp. 626–633, Nov. 1993.

[16] A. Surowiec, S. S. Stuchly, L. Eidus, and A. Swarup, "In-vitro dielectric properties of human tissue at radio frequencies," *Phys. Med. Biol.*, vol. 32, pp. 615–621, May 1987.

[17] M. K. Konings, L. W. Bartels, H. F. M. Smits, and C. J. G. Bakker, "Heating around intravascular guidewires by resonating RF waves," *J. Magn. Reson. Imag.*, vol. 12, pp. 79–95, Jul. 2000.

[18] W. R. Nitz, A. Oppelt, W. Renz, C. Manke, M. Lenhart, and J. Link, "On the heating of linear conductive structures as guidewires and catheters in interventional MRI," *J. Magn. Res. Imag.*, vol. 13, pp. 105–114, Jan. 2001.

[19] M. E. Ladd and H. H. Quick, "Reduction of resonant RF heating in intravascular catheters using coaxial chokes," *Magn. Res. Med.*, vol. 43, pp. 615–619, Apr. 2000.

[20] S. Weiss, P. Vernickel, T. Schaeffter, V. Schulz, and B. Gleich, "Transmission line for improved RF safety of interventional devices," *Magn. Reson. Med.*, vol. 54, pp. 182–189, Jul. 2005.

[21] A. Krafft, S. Müller, R. Umathum, W. Semmler, and M. Bock, "B_1 field-insensitive transformers for RF-safe transmission lines," *Magn. Reson. Mater. Phys.*, vol. 19, pp. 257–266, Nov. 2006.

[22] M. M. Ahmad, R. R. A. Syms, I. R. Young, B. Mathew, W. Casperz, S. D. Taylor-Robinson, C. A. Wadsworth, and W. M. W. Gedroyc, "Catheter-based flexible microcoil RF detectors for internal magnetic resonance imaging," *J. Micromech. Microeng.*, vol. 19, art. no. 074011, pp. 1–10, Jun. 2009.

[23] R. R. A. Syms, K. Segkhoonthod, and I. R. Young, "Periodically structured thin-film cables," *IET Proc. Micr. Antennas Propag.*, vol. 5, pp. 1123–1129, Jun. 2011.

[24] R. R. A. Syms, I. R. Young, M. M. Ahmad, M. Rea, C. A. Wadsworth, and S. D. Taylor-Robinson, "Thin-film detector system for internal magnetic resonance imaging," *Sens. Actuators A*, vol. 163, pp. 15–24, Sep. 2010.

[25] T. L. Peck, R. L. Magin, J. Kruse, and M. Feng, "NMR microspectroscopy on 100-μm planar RF coils fabricated on gallium arsenide substrates," *IEEE Trans. Biomed. Eng.*, vol. 41, no. 7, pp. 706–709, Jul. 1994.

[26] J. Dechow, A. Forchel, T. Lanz, and A. Haase, "Fabrication of NMR-microsensors for nanoliter sample volumes," *Microelectr. Eng.*, vol. 53, pp. 517–519, Jun. 2000.

[27] L. Renaud, M. Armenean, L. Berry, P. Kleimann, P. Morin, M. Pitaval, J. O'Brien, M. Brunet, and H. Saint-Jalmes, "Implantable planar RF microcoils for NMR microspectroscopy," *Sens. Actuators A*, vol. 99, pp. 244–248, Jun. 2002.

[28] A.-L. Coutrot, E. Dufour-Gergam, J.-M. Quemper, E. Martincic, J.-P. Gilles, J. P. Grandchamp, M. Matlosz, A. Sanchez, L. Darasse, and J.-C. Ginefri, "Copper micromolding process for NMR microinductors realisation," *Sens. Actuators A*, vol. 99, pp. 49–54, Apr. 2002.

[29] V. Malba, R. Maxwell, L. B. Evans, A. Bernhardt, M. Cosman, and K. Yan, "Laser-lathe lithography—A novel method for manufacturing nuclear magnetic resonance microcoils," *Biomed. Microdevices*, vol. 5, pp. 21–27, Mar. 2003.

[30] D. Ellersiek, S. Harms, F. Casanova, B. Blümich, W. Mokwa, and U. Schnakenberg, "Flexible RF microcoils with integrated capacitor for NMR applications," in *Proc. Micromechanics Eur.*, Göteborg, Sweden, Sep. 4–6, 2005, pp. 256–259.

[31] M. Woytasik, J.-C. Ginefri, J.-S. Raynaud, M. Poirier-Wuinot, E. Dufour-Gergam, J.-P. Grandchamp, O. Girard, P. Robert, J.-P. Gilles, E. Martincic, and L. Darasse, "Characterisation of flexible RF microcoils dedicated to local MRI," *Microsyst. Tech.*, vol. 13, pp. 1575–1580, Jul. 2007.

[32] E. Shamonina, V. A. Kalinin, K. H. Ringhofer, and L. Solymar, "Magneto-inductive waveguide," *Elect. Lett.*, vol. 38, pp. 371–373, Apr. 2002.

[33] M. C. K. Wiltshire, E. Shamonina, I. R. Young, and L. Solymar, "Dispersion characteristics of magneto-inductive waves: Comparison between theory and experiment," *Elect. Lett.*, vol. 39, pp. 215–217, Jan. 2003.

[34] E. Shamonina and L. Solymar, "Magneto-inductive waves supported by metamaterial elements: components for a one-dimensional waveguide," *J. Phys. D. Appl. Phys.*, vol. 37, pp. 362–367, Jan. 2004.

[35] R. R. A. Syms, L. Solymar, I. R. Young, and T. Floume, "Thin film magneto-inductive cables," *J. Phys. D. Appl. Phys.*, vol. 43, art. no. 055102, pp. 1–7, Jan. 2010.

[36] R. R. A. Syms and L. Solymar, "Bends in magneto-inductive waveguides," *Metamaterials*, vol. 4, pp. 161–169, Dec. 2010.

[37] R. R. A. Syms, L. Solymar, and I. R. Young, "Broad-band coupling transducers for magneto-inductive cable," *J. Phys. D. Appl. Phys.*, vol. 43, art. no. 285003, pp. 1–7, Jun. 2010.

[38] R. R. A. Syms, L. Solymar, and I. R. Young, "Periodic analysis of MR-safe transmission lines," *IEEE J. Sel. Topics Quantum Electron*, vol. 16, no. 2, pp. 433–440, Mar./Apr. 2010.

[39] E. Y. Wong, Q. Zhang, J. L. Duerk, J. S. Lewin, and M. Wendt, "An optical system for wireless detuning of parallel resonant circuits," *J. Magn. Reson. Imag.*, vol. 12, pp. 632–638, Oct. 2000.

[40] S. Weiss, T. Kuehne, F. Brinkert, G. Krombach, M. Katoh, T. Schaeffter, R. W. Guenther, and A. Buecker, "In vivo safe catheter visualization and slice tracking using an optically detunable resonant marker," *Magn. Reson. Med.*, vol. 5, pp. 860–868, Oct. 2004.

Richard R. A. Syms (SM'02) received the B.A. degree in 1979 and the D.Phil. degree in 1982 from Oxford University, Oxford, U.K., both in engineering science.

He is currently a Professor of Microsystems Technology in the Department of Electrical and Electronic Engineering, Imperial College London, London, U.K., where he leads the Optical and Semiconductor Devices Group.

Dr. Syms has published more than 200 journal and conference papers on volume holography, guided wave optics, electromagnetic theory, microelectromechanical systems, and metamaterials. He is a Fellow of the Royal Academy of Engineering, the Institute of Electrical Engineers, and the Institute of Physics.

Ian R. Young received the B.Sc. degree in 1954 and the Ph.D. degree in 1958 from Aberdeen University, Aberdeen, U.K., both in Physics.

He is currently a Senior Research Fellow in the Department of Electrical and Electronic Engineering, Imperial College London, London, U.K. He has published more than 300 papers on MRI. His current interests include *in-vivo* MRI and MR-guided surgical robots.

Dr. Young is a Fellow of the Royal Society and the Royal Academy of Engineering, and winner of the Gold Medal of SMRM and the Sir Frank Whittle Prize.

Munir M. Ahmad received the B.Sc. degree in 1967, M.Sc. degree in 1970 from the University of Punjab, Punjab, India, and the Ph.D. degree in 1978 from the University of Bradford, Bradford, U.K., all in chemistry.

He is currently a Research Fellow in the Department of Electrical and Electronic Engineering, Imperial College London, London, U.K., with special responsibility for clean room facilities. He has been involved for many years in the development of miniature sensing devices, including MEMS mass spectrometers and imaging probes for MRI.

Simon D. Taylor-Robinson received the M.B.B.S. degree in 1984 from the University of London, London, U.K.

He is currently the Director of the Hepatology Clinical Research Facility at St Mary's Hospital, Paddington, London, U.K., and has built up the largest dedicated viral hepatitis treatment center in Europe with an integrated approach to patient care with antiviral therapy, translational research and international, multicentre clinical trials. He is the Dean of the Faculty of Medicine of Imperial College London, London, with a significant role in maintaining academic standards. He also has research programs looking into progression of liver fibrosis and has collaborated with the Engineering Faculty at Imperial on EPSRC, Wellcome, and NIHR grants to produce new medical imaging devices.

Marc Rea received the Ph.D. degree in MR-compatible systems for prostate biopsy from Imperial College London, London, U.K., in 2010.

He is currently a Clinical Scientist at St. Mary's Hospital, London. His research interests include medical robotics, MRI-compatible device tracking, and high-intensity focused ultrasound.